Patterns

A deep-learning method for the end-to-end prediction of intracranial aneurysm rupture risk

Graphical abstract

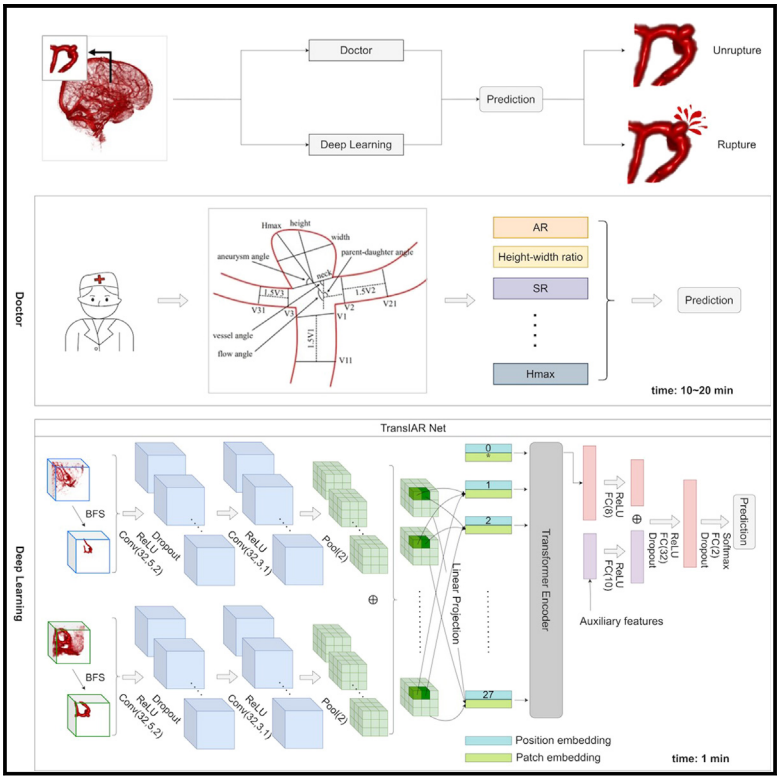

Highlights

- TransIAR net is proposed for predicting rupture status of intracranial aneurysm
- It can be applied to CTA images directly without manually measured features
- A clinical study demonstrates its high accuracy and efficiency
- It outperforms traditional methods and related 2D/3D methods

Authors

Peiying Li, Yongchang Liu, Jiafeng Zhou, ..., Jieqing Wan, Yunjun Yang, Lei Xu

Correspondence

tushikui@sjtu.edu.cn (S.T.), yyjunjim@163.com (Y.Y.), leixu@sjtu.edu.cn (L.X.)

In brief

Effective rupture risk assessment of intracranial aneurysms can greatly reduce aneurysm mortality. Li et al. propose TransIAR net for end-to-end prediction of the rupture status of intracranial aneurysms without laborious human efforts on hand-crafted morphological features. Its performance is better than that of traditional methods and related 2D or 3D methods. In clinical experiments, it achieves higher accuracy and is faster than manual measurements by doctors.

Li et al., 2023, Patterns *4*, 100709
April 14, 2023
https://doi.org/10.1016/j.patter.2023.100709

CellPress

Patterns

CellPress
OPEN ACCESS

Article

A deep-learning method for the end-to-end prediction of intracranial aneurysm rupture risk

Peiying Li,[1,5] Yongchang Liu,[1,5] Jiafeng Zhou,[2,5] Shikui Tu,[1,6,*] Bing Zhao,[3] Jieqing Wan,[3] Yunjun Yang,[2,*] and Lei Xu[1,4,*]
[1]Department of Computer Science and Engineering, Shanghai Jiao Tong University, Shanghai 200240, China
[2]Department of Radiology, The First Affiliated Hospital of Wenzhou Medical University, Wenzhou, Zhejiang 325000, China
[3]Department of Neurosurgery, Ren Ji Hospital, Shanghai Jiao Tong University School of Medicine, Shanghai 200127, China
[4]Guangdong Institute of Intelligence Science and Technology, Zhuhai, Guangdong 519031, China
[5]These authors contributed equally
[6]Lead contact
*Correspondence: tushikui@sjtu.edu.cn (S.T.), yyjunjim@163.com (Y.Y.), leixu@sjtu.edu.cn (L.X.)
https://doi.org/10.1016/j.patter.2023.100709

THE BIGGER PICTURE An intracranial aneurysm (IA) is a pathological expansion of a weak area of a blood vessel wall in the brain because of the long-term effects of abnormal blood flow. Epidemiological estimates suggest that approximately 3% of the population has an intracranial aneurysm. While rupture is rare (occurring in less than 1% of cases), a ruptured IA has a high chance of leading to death. Treatments such as endovascular coiling, a technique that involves navigating a tiny wire coil into the aneurysm, and surgical clipping can reduce the risk of rupture but carry their own risks, including possible death. There is hope that artificial intelligence combined with advanced medical imaging techniques may be able to better identify IAs at high risk of rupture to help prioritize use of these treatments. Here, we describe a machine-learning technique we developed to predict rupture risk from 3D computed tomography angiography data, a medical imaging technique that involves injecting dyes into the blood and then imaging vascular features via X-ray and computational reconstruction. We show that this machine-learning method performs better than human-based predictions within our test datasets, and we hope that this work and others like it will help eventually move these methods into clinical practice, improving treatment outcomes for patients with IA.

Proof-of-Concept: Data science output has been formulated, implemented, and tested for one domain/problem

SUMMARY

It is critical to accurately predict the rupture risk of an intracranial aneurysm (IA) for timely and appropriate treatment because the fatality rate after rupture is 50%. Existing methods relying on morphological features (e.g., height-width ratio) measured manually by neuroradiologists are labor intensive and have limited use for risk assessment. Therefore, we propose an end-to-end deep-learning method, called TransIAR net, to automatically learn the morphological features from 3D computed tomography angiography (CTA) data and accurately predict the status of IA rupture. We devise a multiscale 3D convolutional neural network (CNN) to extract the structural patterns of the IA and its neighborhood with a dual branch of shared network structures. Moreover, we learn the spatial dependence within the IA neighborhood with a transformer encoder. Our experiments demonstrated that the features learned by TransIAR are more effective and robust than handcrafted features, resulting in a 10% – 15% improvement in the accuracy of rupture status prediction.

INTRODUCTION

An intracranial aneurysm (IA) is a pathological expansion of a weak area of an intracranial vessel wall because of the long-term effects of abnormal blood flow. The development of IAs is influenced by vessel wall-related factors, leading, e.g., to a higher prevalence for individuals with polycystic kidney disease (PKD)[1,2] and Ehlers-Danlos syndrome (EDS) type IV.[3,4] Local vascular wall

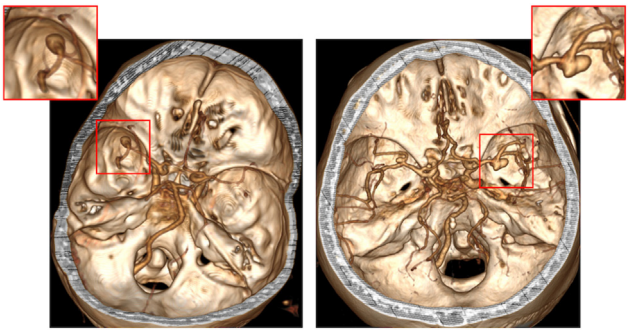

Figure 1. Visualization of IAs

Aneurysms are small and difficult to find. The top left and right corners show enlarged views of the aneurysms.

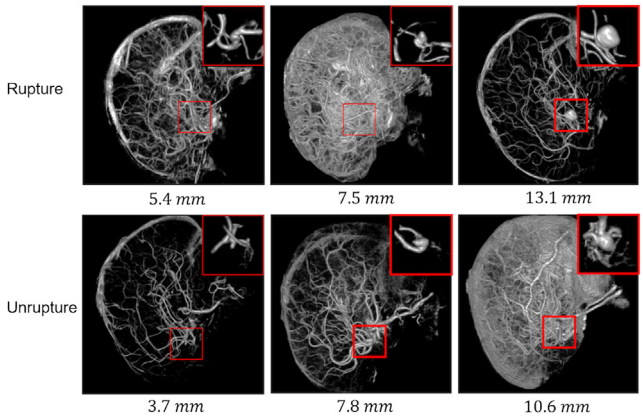

Figure 2. Visualization of IAs

It is difficult to assess whether rupture occurred from the size of the IA. The first and second row show ruptured and unruptured IAs, respectively, and their sizes. The top right corner of each image is a magnified view of the IA.

damage of IAs may be caused by congenital dysplasia or acquired injury to intracranial arteries. The prevalence of IAs in the population is approximately 3.2%,[5] and the probability of aneurysm rupture ranges from 0.25%–0.50%.[6–8] When an aneurysm ruptures, it results in a fatality rate of more than 50%.[9–12] The results of the International Subarachnoid Aneurysm Trial (ISAT) demonstrated that coil embolization can be used to prevent aneurysm bleeding.[13,14] Later, it was also proven in practice that coiling and surgical clipping can avoid the risk of aneurysm rupture while having an acceptable level of safety. The amount of experience of treating aneurysms continues to increase, and equipment upgrades and safety improvements continue to be achieved. Therefore, rapid screening and localization of aneurysms and effective risk assessment can greatly reduce aneurysm mortality. Unruptured IAs, when diagnosed to be low risk, can be treated conservatively, avoiding the risks of surgery (such as death). IAs with impending rupture can be controlled to avoid major bleeding because of rupture.

Bo et al.[15] proposed a deep-learning model for IA detection and segmentation using modern imaging technologies, such as computed tomography angiography (CTA), without manual intervention. As shown in Figure 1, we used the RadiAnt DICOM Viewer software (http://www.radiantviewer.com/) to display intracranial CTA. The aneurysm itself is very small compared with the whole skull, so it is challenging to assess the status of rupture. Related studies have shown that rupture events can be predicted according to the morphological characteristics of aneurysms,[16–20] including aneurysm geometry variables and surrounding vasculature, such as aneurysm size, neck size, aneurysm height, vertical height, aspect ratio, size ratio, vessel angle, anterior projection, irregularity shape, vessel size, and aneurysm angle.[21]

Existing methods for predicting the status of IA rupture can be classified into three types: threshold-based methods, manual feature-based methods, and 2D convolutional neural network (CNN)-based methods. Threshold-based methods predict the rupture status by comparing a feature, such as the aspect ratio or size ratio, with a threshold. The IA aspect ratio is the ratio of IA height to aneurysm neck width. The study[18] found that the larger the aspect ratio, the greater the risk of aneurysm rupture. Various aspect ratio thresholds have been proposed in previous research works[18–20] (e.g., 1.77, 1.18, and even 0.98), and the reason for this is that the rupture event is not absolutely determined by a single risk factor. We visualized examples of ruptured and unruptured IAs in Figure 2. There is a significant overlap between the sizes of the two IA categories. In addition, the thresholds for rupture of aneurysms in different locations are different. For example, the threshold for anterior communicating aneurysms is relatively low. Therefore, there is no consensus on the optimal threshold for the aspect ratio. The IA size ratio is the ratio of the height of the aneurysm to the mean vessel diameter, which is related not only to the size of an aneurysm but also the diameter of nearby local vessels. The determined size ratio thresholds for the height of an aneurysm and the mean vessel diameter[19,22] are 2.05 and 1.5, respectively. Wang et al.[20] reported that the size ratio threshold of posterior communicating artery aneurysm rupture is 1.21. There is a gap between these thresholds. However, it is not surprising that the single-feature thresholds are different in various settings because the rupture risk is affected by several complicated factors.

Manual feature-based methods assess IA rupture status by building traditional machine-learning models, such as support vector machine (SVM), on morphological features that are measured manually and on patient auxiliary features. Elsharkawy et al.[23] and Liu et al.[24] proposed that morphological features and patient-related auxiliary features are related to rupture, and the former are manually measured by neuroradiologists, including aneurysm size, size ratio, aspect ratio, blood flow angle, etc.,[25–30] while the latter are usually related to age, sex, hypertension, smoking history, and other factors.[23,24] Liu et al.[31] used a two-layer feedforward neural network for prediction. In total, 594 IAs (54 unruptured and 540 ruptured) were collected, with 13 morphological features and 4 statistical features as input. Zhu et al.[32] collected 13 patient-specific clinical features and 18 aneurysm morphological features as input data for machine-learning models; e.g., SVM, random forest (RF), and feedforward artificial neural network (ANN).

In addition to manually measuring features, alternative methods of automatically extracting features exist. Raghavan et al.[18] proposed automatically determining the size and shape index of IAs to distinguish between ruptured aneurysms and unruptured aneurysms, which requires semiautomatic

segmentation followed by automatic parameterization. Detmer et al.[33,34] collected 1,631 IAs and related features, including hemodynamic, morphological, and patient-related information, to predict IA rupture status. They automatically obtained 22 hemodynamic and 25 morphological parameters of IAs through computational fluid dynamics simulations. Although these methods determine some parameters automatically, they are limited to parameterization of aneurysm features to train the classifier.

The methods relying on morphological features measured by neuroradiologists or automatic measurement of limited features to predict rupture status are time consuming, labor intensive, and limited. Measurement of morphological features is based on visualization software, which reconstructs and stereoscopically presents CTA vascular images, as shown in Figure 1. However, at present, CTA imaging technology is less sensitive for small aneurysms[35] with a maximum diameter $< 3\ mm$, and there are still cases of missed diagnosis. The software cannot fully display the aneurysm and surrounding blood vessels. Moreover, neuroradiologists may be at different proficiency levels, and manual measurement is subjective to some extent, which may induce wide variations and uncertainties in the data. In this paper, we aim to build an end-to-end model to automatically learn the morphological features of IAs from CTA images without the involvement of neuroradiologists and visualization software.

2D CNN-based methods utilize the 2D CNN network to extract features from 2D IA images to assess rupture status. In a recent study, Kim et al.[9] used 2D aneurysm images rather than manually measured features to predict rupture status, collecting a total of 640 patients with IAs, of which 368 patients were used in the training set. They captured 2D images of IAs in six directions and then performed data augmentation to expand the dataset, adopting Alexnet_v2 as the backbone for training, and the model was finally tested in the remaining 272 patients. Although the 2D images have an edge over manually measured features, the 2D projections introduce information loss and lead to limited features. The proposed method in this paper works directly on the 3D CTA image, and the learned features are more comprehensive.

Existing methods for predicting rupture status usually take multiple morphological features to build prediction models,[21] and the morphologies are manually measured by neuroradiologists with the assistance of machines. This paradigm has the following limitations. First, it demands that experienced neuroradiologists spend much time performing measurements. Second, various standards of different neuroradiologists may induce large variations and uncertainties in the data. Third, other unknown important features may have been missed or difficult to craft by neuroradiologists; for example, studies have found that the perianeurysmal environment of an IA has a certain influence on the risk of rupture.[36]

The existing methods mainly focus on the morphological features of an IA and barely consider the aneurysm's surrounding information. Several studies have found that the perianeurysmal environment of the IA also has a certain influence on the risk of rupture. Sugiu et al.[36] introduced the term "perianeurysmal environment" to group the anatomical structures, including the brain, dura, bone, vessels, and nerves surrounding IAs, whose influence on IAs was considered to be balanced or unbalanced according to symmetric or asymmetric forces exerted by those structures, respectively. They found that the perianeurysmal environment has a significant influence on aneurysmal growth, shape, and rupture pattern. Compared with unruptured IAs, ruptured IAs have more contact with the perianeurysmal environment, which is more likely to be unbalanced. The irregular shape was proven to have a positive correlation with unbalanced contact.[37] Backes et al.[38] concluded that whether the high risk of rupture was caused by contact or by aneurysm size is undefined. Because large aneurysms are more likely to be in contact with the environment because of the limited local subarachnoid space, the relationship between large aneurysm size and rupture cannot be considered in isolation. In other methods based on manual features, the analyses of some other parameters (including shape) also have similar problems. Therefore, it is challenging to measure the complex influence of these risk factors on rupture. In this paper, we address this challenge and incorporate IA neighborhood information for rupture prediction using a deep-learning method. Our method features a multiscale CNN for learning scale-invariant representations of an IA and its neighborhood and a transformer for neighborhood representation enhancement.

In recent years, medical imaging has witnessed great development thanks to deep learning, and progress has been made in cell segmentation,[39] organ segmentation,[40,41] and aneurysm detection and segmentation.[42–44] Deep representation learning creates opportunities to address the limitations of measuring morphological features manually by neuroradiologists. However, there are two challenges. First, the geometric shapes of IAs are usually irregular in 3D CTA data, and IAs may appear in various directions and sizes. Second, the IA neighborhood (e.g., the perianeurysmal environment), which is rarely taken into account in existing methods, needs to be considered in deep representation learning for more features than hand-crafted ones because it has a complicated impact on the rupture risk.

In this paper, we propose an end-to-end deep-learning method, called TransIAR net, to tackle the above two challenges. Our method takes the 3D CTA data as the input and extracts the risk-related structural features automatically for accurate rupture status prediction. To the best of our knowledge, TransIAR net is the first end-to-end method for IA rupture prediction. The main contributions are summarized below.

- We propose a multiscale 3D CNN to automatically extract morphological features from CTA images. The 3D scale-invariant, risk-related embedding is captured from not only the 3D IA itself but also its cubic neighborhood.
- We further learn the spatial dependence within the IA neighborhood by cutting the 3D CNN embeddings into small feature cubes and modeling the cubes in order with a transformer encoder. Then, the long-range dependencies on the IA and the geometry of the surrounding blood vessels result in more discriminative features.
- We evaluate the effectiveness of TransIAR on balanced and unbalanced datasets. The results show that TransIAR outperforms the existing methods in terms of accuracy, precision, recall, area under the curve (AUC), area under the precision-recall curve (AUPR), and F1 score. Moreover, the computed embeddings by TransIAR are better than the features measured by neuroradiologists when feeding them into an RF or SVM model

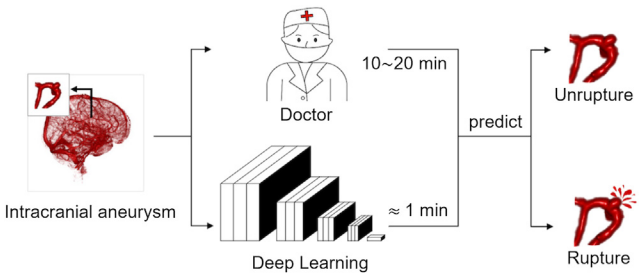

Figure 3. Comparison of diagnosis time for a doctor and our deep-learning method

for rupture status prediction. In addition, as given in Figure 3, it takes approximately 2 min for our deep-learning method to preprocess the data and make the prediction, while neuroradiologists may take approximately 20 min on average (this was determined by collecting the time used by five neuroradiologists on 10 randomly selected cases in the First Affiliated Hospital of Wenzhou Medical University), which is 10 times longer, to measure the morphologies and use the existing models for prediction.

RESULTS

Data preparation

We collected CTA images of 556 patients with IAs from hospital A from January 2009 to December 2019. The CTA images are stored in DICOM (Medical Digital Imaging and Communication) format. The hospital uses three multidetector CT scanners to collect intracranial data: (1) Aquilion ONE (Toshiba Medical Systems, Japan), (2) Lightspeed VCT 64 (General Electrical Medical Systems, Milwaukee, WI, USA), and (3) Lightspeed pro16 (General Electrical Medical Systems). Correspondingly, the section thicknesses are 0.5 mm, 0.625 mm, and 1.25 mm; the reconstruction intervals are 0.5 mm, 0.625 mm, and 1.25 mm; the tube voltages are 100 kV, 100 kV, and 120 kV; the tube currents are 300 mA, 500 mA, and 300 mA; and the matrix sizes are the same (i.e., 512 × 512).

The data inclusion criteria were as follows: (1) patients with one or more IAs and (B) cystic aneurysms. The data exclusion criteria were as follows: (1) aneurysms with a diameter less than 3 mm, (2) poor CTA image quality, (3) patients receiving surgical or interventional treatment before CTA, and (4) multiple aneurysms and failure to identify which ruptures. Finally, 423 patients with 449 IAs (ruptured and unruptured) were retained as an internal dataset. They were divided into internal training and test sets.

The IA annotation criteria are as follows. (1) An aneurysm is annotated as "ruptured" when its CT plain scan or cerebrospinal fluid examination shows subarachnoid hemorrhage (SAH), which is confirmed by CTA, DSA or surgery. (2) The remaining aneurysms are annotated as "unruptured."

The collected dataset is an imbalanced dataset consisting of 141 cases of unruptured IAs and 308 cases of ruptured IAs, as shown in Table 1. To better train and test the model, we conduct experiments under balanced and imbalanced settings. For the balanced setting, we randomly selected a completely balanced dataset for training and testing. The numbers of ruptured IAs and unruptured IAs are the same in the training set and testing set. To test the robustness of the model, we added an independent set of unused 167 cases of ruptured IAs to the balanced test set and retested the performance of the model. The size distribution of aneurysms is given in Table 2. The dataset covers all sizes, with small aneurysms (< = 4 *mm*) accounting for 19% in the training set and 15.8% in the testing set.

Table 1. Statistics about collected CTA imbalanced dataset and balanced dataset

	Imbalanced dataset			Balanced dataset		
State	Training	Testing	Total	Training	Testing	Total
Ruptured	100	208	308	100	41	141
Unruptured	100	41	141	100	41	141
Total	200	249	449	200	82	282

To verify the generalization of our model, we also collected CTA data from four other hospitals and merged them as an external test set. The inclusion and exclusion criteria are the same as those of the internal dataset. There is no intersection between the internal dataset and the external test set. The external test set contains 43 CTA images with 14 unruptured IAs and 29 ruptured IAs. Details about the external test set can be seen in supplemental experimental procedures section S1.

To enhance the model training, data augmentation is conducted for the training and testing data. Each input data cube is augmented to have 32 different variants by randomly rotating the cube by a certain angle in the x, y, and z directions. Note that, to prevent the loss of information during rotation, we first cut the cube slightly larger than our target size and cut the cube of the target size from the center of the rotated cube.

Morphological and auxiliary features are based on ruptured and unruptured IAs. Group A is the set of features hand-crafted by neuroradiologists who are familiar with CTA image reconstruction and measurement, and group B is the set of features that can be easily obtained, called auxiliary features (AFs). The p values were calculated by t tests and chi-square tests with Bonferroni correction.

In addition, we collected the clinical information of the patients and the basic morphological parameters of the aneurysm, as listed in Table 3. We divided these features into two groups, A and B. Group A contained features that require neuroradiologists familiar with CTA image reconstruction and measurement, and group B contained features that can be obtained easily, such as age, shape, and location. In this paper, we used group A as hand-crafted IA features and group B as AF s. As in the literature, e.g., Chen et al.,[21] we assessed the statistical significance of the association between each feature and the rupture status. In detail, we used the t test for continuous features and the chi-square test for categorical features, after which we adjusted the p values by Bonferroni correction. Features with a p value less than 0.05 were considered statistically significant. Notably, all features of group A and group B were significantly associated with the rupture

Table 2. Statistics about IA size

	< = 4 mm	4 mm – 7 mm	> 7 mm
Training	38	78	84
Testing	13	38	31

Table 3. Morphological and AFs based on ruptured and unruptured IAs

Group	Features	Ruptured	Unruptured	p Value
A	AR	1.14 ± 0.54	0.86 ± 0.59	2.96E−07
	height-width ratio	0.89 ± 0.25	0.77 ± 0.26	1.06E−06
	SR	2.69 ± 1.61	1.94 ± 1.56	2.08E−06
	Hmax (mm)	5.77 ± 2.92	4.45 ± 2.98	7.85E−06
	BNF	1.3 ± 0.54	1.09 ± 0.52	0.000196
	Vessel size (mm)	2.3 ± 0.5	2.46 ± 0.55	0.013133
	Size (mm)	7.42 ± 3.29	6.44 ± 3.34	0.019203
	H (mm)	4.68 ± 2.54	3.9 ± 2.83	0.020827
B (AF)	Shape			2.98E−09
	Regular	42.36%	70.42%	
	Irregular	57.63%	29.57%	
	Daughter domes			8.14E−06
	No	68.42%	87.79%	
	Yes	31.57%	12.20%	
	Multiple aneurysms			8.23E−06
	Single	81.12%	61.17%	
	Multiple	18.88%	38.83%	
	Location			0.000444
	M1-LSAAs	1.58%	7.98%	
	M1-EFBAs	14.21%	18.31%	
	M1-ETBAs	10.26%	9.86%	
	MbifAs	71.58%	56.81%	
	MdistAs	2.37%	7.04%	
	Age (years)	56.28 ± 11.49	60.66 ± 11.99	0.000602

Group A is a set of hand-crafted features by neuroradiologists who are familiar with CTA image reconstructions and measurements, and Group B is a set of features that can be easily obtained, called auxiliary features (AFs). The p values are calculated by t test (for continuous features) and chi-square test (for categorical features) with Bonferroni correction. The calculation details of the p value can be found in the Supplemental Experimental Procedures Section S5. The full names and definitions of abbreviations are shown in the Supplemental Experimental Procedures Section S7.

status. Continuous features are presented as the mean ± standard deviation, and categorical features are presented as percentages. The features were processed using the Standard Scaler, which normalized the features by the variance.

Results compared with those of existing methods

Automatically extracted features vs. manually extracted features

Existing methods usually use features (e.g., aneurysm size, height, parent artery width) measured manually by neuroradiologists as input and train traditional machine-learning models such as SVM and RF to predict the rupture status. The proposed TransIAR net is able to learn aneurysm features in an end-to-end manner in the absence of neuroradiologists. In the following, we evaluate the predictive performance of our automatically extracted features in comparison with that of the human-measured features.

We implement RF and SVM from the existing methods as baselines. We use the manually measured features (i.e., group A in Table 3), as input to train an RF or SVM, and the trained models are denoted as RF^m or SVM^m. For fair and comprehensive comparison, we build models from automatically extracted features under three scenarios: (1) RF^a and SVM^a, an RF and an SVM classifier that are trained on the 8-dimensional features learned by our TransIAR net; (2) IAR net, which is trained in an end-to-end manner using TransIAR net without activating the transformer module; and (3) TransIAR net, the proposed end-to-end deep-learning model.

The prediction performance is listed in Table 4. We see that RF^a and SVM^a outperform RF^m and SVM^m, respectively, by a large margin in all evaluation indicators. For example, the prediction accuracy of SVM^a is 89.02%, approximately 10% higher than that of SVM^m. The features extracted via TransIAR are much more effective and discriminative than the hand-crafted features, which indicates that TransIAR net is capable of breaking through the limitations of feature engineering by neuroradiologists. SVM is generally better than RF on both types of features. The prediction AUC or AUPR is further improved by TransIAR net over SVM^a when representation learning and classifier building are jointly optimized in one model.

It can be concluded that IAR outperforms RF^m and SVM^m but is inferior to RF^a and SVM^a. The representation learning of IAR net mainly relies on the multiscale 3D CNN in the BranchNet module when the transformer module is removed. The results indicate that the multiscale 3D CNN alone is effective in extracting features for rupture prediction, and the transformer module further enhances representation learning by exploiting the contextual dependence within the IA neighborhood.

TransIAR vs. 2D and 3D models

We consider relevant state-of-the-art (SOTA) 2D or 3D models in the literature and reproduce them for comparison. The training details can be found in supplemental experimental procedures section S2. It should be noted that the existing 3D models are not for the prediction problem of IA rupture status, and thus we modify them appropriately to adapt to the problem setting in this paper. First, we reimplemented the network of Kim et al.,[9] which used a 2D method to predict the rupture status of aneurysms. Kim et al.[9] captured aneurysm images in six directions (front and back, both sides, and top and bottom), and then the neuroradiologists selected the region of interest, including the aneurysm, as the network input.

Second, we reimplemented the M3T[45] 3D network for comparison. The M3T network was originally developed by combining 3D CNN, 2D CNN, and transformer to classify Alzheimer's disease (AD) on 3D MRI (magnetic resonance imaging) images. We slightly modify the M3T network to take CTA images as input and train it on our CTA data.

Finally, we considered a 3D U-Net model, called DAResUNET,[42] which was originally proposed for aneurysm segmentation. As shown in Figure S1A, a dual attention block (DAB) at the bottleneck of 3D U-Net is added to model the semantic relationship of the spatial and channel dimensions of IAs. Because DAResUNET was originally developed for aneurysm segmentation, it needs to be adjusted for rupture status prediction. As illustrated in Figure S1A, DAResUNET, published in GitHub (https://github.com/deepwise-code/DLIA) by the original author, is a typical U-Net architecture with an encoder and a decoder as well as skip connections from the encoder to decoder. We include two versions of DAResUNET for comparison. One is given in Figure S1B and

Table 4. The results on the balanced test set

Models	Feature	Accuracy (95% CI)	Precision	Recall	AUC	AUPR	F1 score
RF^m	manual (group A)	74.39 (64.94–83.84)	68.52	*90.24*	83.58	81.48	77.89
SVM^m	manual (group A)	79.27 (70.50–88.04)	81.58	75.61	85.46	82.57	78.48
RF^a	auto (by TransIAR)	84.15 (76.25–92.05)	80.43	*90.24*	88.34	90.88	85.06
SVM^a	auto (by TransIAR)	*89.02 (82.25–95.79)*	*88.10*	*90.24*	91.23	91.68	*89.16*
Kim et al.[9]	auto	79.27 (70.50–88.04)	81.58	75.61	85.07	78.86	78.48
M3T[45]	auto	85.37 (77.72–93.02)	87.18	82.93	87.92	89.05	85.00
DAResUNET^b [42]	auto	84.15 (76.25–92.05)	80.43	*90.24*	89.89	90.37	85.06
DAResUNET^c [42]	auto	84.15 (76.25–92.05)	85.00	82.93	91.97	91.12	83.95
IAR	auto (by IAR)	82.93 (74.79–91.07)	81.40	85.37	88.22	88.95	83.33
TransIAR	auto (by TransIAR)	*89.02 (82.25–95.79)*	*88.10*	*90.24*	*92.15*	*93.16*	*89.16*

"Manual" and "auto" indicate models trained with manually extracted features or automatically extracted features, respectively. RF^m and SVM^m are trained with group A setting features. The 95% confidence interval (CI) denotes the binomial proportion CI at the significance level of 95%. The best results are shown in bold. The calculation details of CI are shown in Supplemental Experimental Procedures Section S4.

denoted DAResUNET^b, which only uses the encoder and DAB of DAResUNET as the skeleton and a simple classifier composed of multilayer perceptron (MLP) at the tail. Cross-entropy loss is used to train the model. The other is shown in Figure S1C and denoted DAResUNET^c. It uses the original DAResUNET structure to extract features in the bottleneck layer by minimizing a reconstruction loss by the mean square error (MSE) function and adopts an MLP classifier on the bottleneck layer features.

As reported in Table 4, the results of these models on the balanced test set demonstrate that TransIAR is the best under almost all metrics, while DAResUNET^b demonstrates its relative strength in terms of recall score. We visualized two examples from misclassified samples of TransIAR in supplemental experimental procedures section S6.

We released the code and the trained models of the above methods on GitHub (https://github.com/CMACH508/TransIAR).

Results on the imbalanced test set

To demonstrate the models' robustness, we test the models based on the imbalanced test set, which has five times more ruptured IAs than unruptured IAs. The results are reported in Table 5. Generally, the IA features learned by TransIAR net are more effective than the manually measured morphological features. The TransIAR net, which jointly optimizes representation learning and classifier construction, greatly outperforms the existing methods (RF^m and SVM^m). Again, the AF s are consistently beneficial to improve the prediction performance of all models (except RF), playing a similar role under the balanced setting.

Table 5 shows that RF is more robust than SVM under the imbalanced setting. The features learned by TransIAR net enable RF and SVM to bridge the gap and become comparable with TransIAR net.

We observe that the recent popular 2D or 3D classification models achieve much higher accuracy than methods of manually extracting features (i.e., RF^m, SVM^m). On the imbalanced test set, TransIAR is the best under the Precision, AUC, and AUPR metrics. The 3D methods (M3T, DAResUNET^b, and DAResUNET^c) also exceed RF^m and SVM^m, but they are still inferior to TransIAR.

The impact of AFs

When neuroradiologists assess the rupture risk of an aneurysm, they not only check the 3D reconstruction of a CTA vascular image through software but also take AFs into consideration, such as patient age and aneurysm location. As shown in Table 3, the AFs are indeed significantly associated with the rupture status, but they may not be easily learned from the CTA image. It would be beneficial to include the AFs for rupture prediction. The benefit is first confirmed by the experiments on the baseline methods in Table 6. With the AFs, the prediction accuracy of RF^m and SVM^m increases by 6.10% and 4.88%, respectively.

The results of including the AFs in the training under balanced and imbalanced settings are reported in Tables 7 and 8. Comparing Tables 4 and 7, the incorporation of AFs further improves the accuracy of IAR by 1.22% and TransIAR by 2.44% on the balanced test set and improves the accuracy of IAR by 6.83% and that of TransIAR by 4.42% on the imbalanced test set. The gain by the AFs is as obvious as that for RF^m or SVM^m on balanced and imbalanced test sets. When comparing IAR and TransIAR, the transformer module consistently contributes an improvement on all metrics in the absence of AFs, while the improvement becomes negligible with a slight tendency toward high precision and AUC in the presence of AFs. There is no obvious gain for RF^a or SVM^a. Perhaps it is better to consider the AFs jointly with the deep representation learning on an IA and its neighborhood so that the learned features can be further optimized in a cooperative, complementary manner.

To summarize, the proposed TransIAR net is able to significantly improve the prediction performance over the existing methods; i.e., RF^m and SVM^m. The IA features learned by TransIAR net can also strengthen RF^a and SVM^a to exceed RF^m and SVM^m, respectively. The TransIAR net further improves the prediction accuracy with the assistance of AFs.

Results on the external test set

We evaluate our model and other compared methods on the external test set, as shown in Table 9. TransIAR is better than or the same as traditional methods (RF^m, SVM^m), 2D methods (Kim et al.[9]), and 3D methods (M3T, DAResUNET^b, and DAResUNET^c) in performance on all metrics. To summarize, the results are consistent with those on the internal test set. TransIAR has been demonstrated to have good generalization performance.

Comparisons with MaSIF-Net and Triangle-Net for automatic feature extraction

There exist other deep-learning methods that are able to automatically extract features from 3D data. molecular surface

Table 5. The results on the imbalanced test set

Models	Feature	Accuracy (95% CI)	Precision	Recall	AUC	AUPR	F1 score
RF^m	manual (group A)	74.70 (69.30–80.10)	90.50	77.88	75.32	93.40	83.72
SVM^m	manual (group A)	60.24 (54.16–66.32)	94.31	55.77	77.37	93.59	70.09
RF^a	auto (by TransIAR)	**83.53** (78.92–88.14)	95.14	**84.62**	86.73	97.19	**89.57**
SVM^a	auto (by TransIAR)	79.92 (74.94–84.90)	97.02	78.37	88.44	97.28	86.70
Kim et al.[9]	auto	73.49 (68.01–78.97)	95.51	71.63	85.20	94.57	81.87
M3T[45]	auto	79.12 (74.07–84.17)	96.99	77.40	88.90	97.26	86.10
$DAResUNET^b$ [42]	auto	80.32 (75.38–85.26)	94.92	80.77	87.27	97.03	87.27
$DAResUNET^c$ [42]	auto	77.11 (71.89–82.33)	96.32	75.48	88.57	97.14	84.64
IAR	auto (by IAR)	78.31 (73.19–83.43)	95.29	77.88	85.96	96.70	85.71
TransIAR	auto (by TransIAR)	80.72 (75.82–85.62)	**97.06**	79.33	**89.28**	**97.57**	87.30

The labels "manual" and "auto" indicate models trained with manually extracted features or automatically extracted features, respectively. RF^m and SVM^m are trained with group A setting features. The best results are shown in bold.

interaction fingerprinting (MaSIF) (https://github.com/LPDI-EPFL/masif), a recent deep geometric learning method, has been proven to be effective in deciphering interaction patterns from the 3D protein's molecular surface.[46] It computes a descriptor for each surface patch according to geometric features and captures the fingerprints for specific biomolecular interactions. Inspired by MaSIF, we removed the internal points of the segmented aneurysm annotated by neuroradiologists and constructed a mesh on the IA surface. Around each vertex of the mesh, a patch with a fixed geodesic radius is extracted, and for each vertex in the patch, two geometric features are calculated; namely, shape index and distance-dependent curvature. Because of memory limitations, 64 patches randomly selected from the aneurysm surface were utilized as the input of MaSIF Net. Finally, we obtained a predicted score for aneurysm rupture status. Under the balanced dataset, our test accuracy on the constructed aneurysm mesh is 0.6951, which is poorer than the existing methods, RF^m and SVM^m, as shown in Table 4. Additionally, we include an experiment to investigate the effects of the number of patches on the performance. More details can be found in supplemental experimental procedures section S3.

Triangle-Net[47] is another effective deep-learning method for point cloud learning, with an invariance property against rotation. It utilizes the graph structure of the point cloud to extract hyperedge features and then uses graph aggregation to obtain latent representation for classification. We process the segmented aneurysm annotated by neuroradiologists, remove the internal points, interpolate and sample, and then feed them into Triangle-Net. The testing accuracy on the balanced dataset is 0.7195, lower than that of RF^m and SVM^m according to Table 4.

The major reason for the poor performance of these two methods is that they can extract the structural and geometric features of the aneurysm itself but fail to learn the detailed information about the nearby blood vessel structure. It is difficult for them to obtain the diameter of the surrounding blood vessel, the angle of blood flow, the width of the aneurysm neck, and other important features that affect the rupture. In contrast, the proposed TransIAR net fully excavates information from aneurysm data in an end-to-end way and optimizes the relationship between data features and rupture status. It achieves a prediction accuracy as high as 89.02% (Table 4), exceeding the existing methods, even in the absence of AFs.

Clinical experiment

To show the clinical applicability of TransIAR, we conducted a clinical experiment to compare the accuracy of doctors and TransIAR net in IA rupture prediction. In clinical experiments, doctors need to predict whether the aneurysm is ruptured according to morphological parameters.

The clinical experimental scheme is as follows. (1) The 3D CTA images and shape parameters are prepared for doctors to predict IA rupture status. It is necessary to comprehensively display the morphological characteristics of the aneurysms and mark the size of the aneurysms. (2) Two doctors (a radiologist and a neurosurgeon) assessed the rupture status of the aneurysms. The "ruptured" IA is annotated as 1, and the "unruptured" IA is annotated as 0. The time each doctor spends is recorded. (3) The results of two doctors with the ground truth labels are compared.

The results of clinical performance are shown in Table 10. We see that TransIAR outperforms doctors in accuracy and AUC in practice. The average time doctors spend is approximately 1 h, and TransIAR spends less than 4 s, which is far less than the time doctors spend.

The impact of the neighborhood of an IA

First, we determine the size of the neighborhood of an IA. A patient's 3D CTA image data usually have $S\times512\times512$ voxels, where S is the patient-specific number of slices, and each slice is a 512×512 image. The distribution of the aneurysm size (i.e., maximum diameter in voxels) is given in Figure 4. In our collected

Table 6. The performance of RF^m and SVM^m when trained on manually extracted features and AFs

Models	Data settings	Accuracy
RF^m	group A	74.39
	group B	69.51
	groups A & B	**80.49**
SVM^m	group A	79.27
	group B	74.39
	groups A & B	**84.15**

The results are evaluated on the balanced test set. The best results are shown in bold.

Table 7. Performance of models trained with additional AFs and tested on the balanced test set

Models	Feature	Accuracy (95% CI)	Precision	Recall	AUC	AUPR	F1 score
RF^m	manual (groups A & B)	80.49 (71.91–89.07)	75.51	90.24	84.41	77.22	82.22
SVM^m	manual (groups A & B)	84.15 (76.25–92.05)	85.00	82.93	87.03	80.79	83.95
RF^a	auto (by TransIAR) & group B	84.15 (76.25–92.05)	80.43	90.24	88.25	89.48	85.06
SVM^a	auto (by TransIAR) & group B	87.80 (80.72–94.88)	86.05	90.24	**93.22**	**92.52**	88.10
IAR	auto (by IAR) & group B	84.15 (76.25–92.05)	78.00	**95.12**	89.83	89.89	85.71
TransIAR	auto (by TransIAR) & group B	**91.46 (85.41–97.51)**	**94.74**	87.80	92.09	89.58	**91.14**

The labels "manual" and "auto" indicate the manually extracted features and the automatically extracted features, respectively. The best results are shown in bold.

dataset, the size of the largest aneurysm was 42 voxels, and the smallest was 5 voxels. The aneurysms are very small compared with the entire intracranial CTA. If the entire brain is regarded as the IA neighborhood, it would be difficult for the model to focus on the tiny aneurysm. Instead, we crop a cube from the 3D CTA around the center of an IA. Because the size of the maximum aneurysm is 42 voxels, we choose 48 voxels as the smallest edge length of the cubic neighborhood to cover the whole aneurysm. For more neighborhood information when the aneurysm is large, we also consider 96 voxels as the edge size of the neighborhood.

The cropped cubic data around the aneurysm centers contain the morphological structure of the IA and its neighborhood with surrounding anatomical structures; e.g., small blood vessels and impurities. The input data include not only the cropped cube but also the cube processed by the breadth first search (BFS) method to obtain the IA and parent arteries. Note that the BFS process removes much neighborhood information from the cropped cubic data. Figure 5 visualizes the preprocessing of the data of the IA and its neighborhood. The cubic neighborhood of 96^3 voxels (in red) is downsampled to 48^3 voxels, which is kept as the input size for the TransIAR net. The cubic data of the third column (before BFS) contain the IA and its neighborhood, while the ones of the fourth column (after BFS) contain the morphology of the IA and its parent arteries. We consider different combinations of cubic data of both columns and evaluate the impact of neighborhood information on the prediction performances in Table 11.

It can be seen in Table 11 that the prediction performance of TransIAR net drops by a large margin when BFS is used to remove much neighborhood information. The performance is better when the neighborhood size is 96. The BFS-derived cubic data, when fed into the network together with the cropped cubic data, are beneficial to improve the prediction performance because they are able to strengthen the representation learning on the IA's geometry features by reducing the disturbance from the neighborhood. The best result is achieved with the combination of all sizes and BFS cases. To summarize, the IA neighborhood information, which has been largely ignored by other existing methods, plays a very important role in rupture status prediction, and the diverse, multiscaled input enhances the deep representation learning on the IA and its neighborhood.

DISCUSSION

The existing machine-learning methods require neuroradiologists to manually measure the characteristics of IA morphology or semiautomatic segmentation followed by automated shape parameterization to predict the status of aneurysm rupture, and the process is time consuming, labor intensive, and limited in feature extraction, and it barely takes into account IA neighborhood information. In this paper, we propose an end-to-end deep-learning method, TransIAR net, for aneurysm rupture prediction. A multiscale deep 3D CNN is developed to automatically extract the morphological features of an IA and its neighborhood information directly from the 3D CTA image data. A transformer module is devised to model the spatial dependence within the 3D CNN embeddings of the aneurysm and its surrounding anatomical structures, and the representation learning is strengthened to be more discriminative and predictive for rupture prediction. We evaluate the TransIAR net by experiments on balanced and unbalanced datasets. The prediction performance becomes much better when the hand-crafted features collected by the neuroradiologists are replaced by the features learned by the TransIAR net in a traditional machine-learning model such as RF or SVM. The performance is further improved when the representation learning and classifier construction are jointly optimized by the TransIAR net. To the best of our knowledge, the TransIAR net is the first end-to-end model with a fast and

Table 8. Performances of models trained with additional AFs and tested on the imbalanced test set

Models	Feature	Accuracy (95% CI)	Precision	Recall	AUC	AUPR	F1 score
RF^m	manual (groups A & B)	72.29 (66.73–77.85)	92.64	72.60	76.90	92.86	81.40
SVM^m	manual (groups A & B)	70.68 (65.03–76.33)	95.92	67.79	82.42	94.52	79.44
RF^a	auto (by TransIAR) & group B	83.13 (78.48–87.78)	96.11	83.17	87.36	97.12	89.18
SVM^a	auto (by TransIAR) & group B	84.34 (79.83–88.85)	96.69	84.13	89.99	**97.66**	89.97
IAR	auto (by IAR) & group B	**85.14 (80.72–89.56)**	94.30	**87.50**	88.63	97.41	**90.77**
TransIAR	auto (by TransIAR) & group B	**85.14 (80.72–89.56)**	**98.86**	83.17	**90.00**	97.27	90.34

The labels "manual" and "auto" indicate the manually extracted features and the automatically extracted features, respectively. The best results are shown in bold.

Table 9. Performance of models on the external test set

Models	Feature	Accuracy (95% CI)	Precision	Recall	AUC	AUPR	F1 score
RF[m]	manual (group A)	65.12 (50.87–79.37)	76.92	68.97	72.66	83.99	72.73
SVM[m]	manual (group A)	58.14 (43.39–72.89)	82.35	48.28	80.05	89.79	60.87
Kim et al.[9]	auto	65.12 (50.87–79.37)	**100.0**	48.28	91.63	96.01	65.12
M3T[45]	auto	76.74 (64.11–89.37)	95.24	68.97	94.09	97.12	80.00
DAResUNET[b] [42]	auto	83.72 (72.69–94.75)	95.83	79.31	94.58	97.54	86.79
DAResUNET[c] [42]	auto	88.37 (78.79–97.95)	**100.0**	82.76	97.29	98.71	90.57
IAR	auto (by IAR)	90.70 (82.02–99.38)	96.30	**89.66**	95.32	97.80	92.86
TransIAR	auto (by TransIAR)	**93.02 (85.40–100.0)**	**100.0**	**89.66**	**98.03**	**99.17**	**94.55**

The best results are shown in bold.

accurate prediction of IA rupture status from 3D CTA data, which is a promising tool to assist doctors in clinical practice.

Moreover, it is convenient to extend our method to be an end-to-end deep-learning method for IA detection and rupture status prediction. Our method takes as input 3D CTA data and a center coordinate of IA location, which can be easily obtained by existing IA detection methods.[15,42,44] With this paradigm, segmenting an IA from 3D CTA data is not necessary. Even when the segmentation of IA morphology is perfect, it is not enough to accurately predict the rupture status because neighborhood information is also valuable and must be supplemented in representation learning. Under the end-to-end extension for detection and rupture status prediction, the two tasks can be jointly implemented. The learning process may benefit from both sides and lead to more interpretable features. We hope that it will help to transform and enhance the clinical diagnostics and precision treatments of cerebrovascular diseases.

Prior to our method, the risk-relevant features, mainly of IA morphology, were usually extracted manually by neuroradiologists. This manual process usually requires approximately 20 min and is limited by geometric distances or angles. Our method not only reduces the time to approximately 2 min but also breaks through the limitations. For example, it effectively captures neighborhood information that is difficult to measure manually. The information tends to be related to the perianeurysmal environment[36] of the IA, which has been largely ignored by existing methods. The perianeurysmal environment is a group of anatomical structures, including the brain, dura, bone, vessels, and nerves surrounding IAs, and studies[36] have found that the perianeurysmal environment has a certain impact on the risk of rupture. Because of the black box characteristics of deep learning, further investigation of the clinical interpretability of deep features is needed, which may provide new insights into rupture risk studies.

It is difficult to learn the representations of the irregular shape of an IA and its complex surrounding environment from 3D CTA data. Deep learning methods, such as MaSIF[46] and Triangle-Net,[47] have been developed to extract features from 3D data in various applications. Although MaSIF or Triangle-Net are easy to adopt to extract the structural and geometric features of an IA, learning information about the nearby vascular structure is very difficult. Moreover, IAs may appear in different sizes and orientations. The proposed multiscale 3D CNN is more effective in meeting these challenges, and the transformer on the CNN embedding space is effective in learning the surrounding information. Comparisons with the state-of-the-art 3D deep networks, including U-Net variants, indicate that the TransIAR net outperforms the existing 3D network structures in addressing the IA rupture prediction problem. However, there is still room for improvement. It would be beneficial to incorporate the recent advances in geometric deep learning and equivariant neural networks.[48,49]

It is noted from the experimental data that the study conducted in this paper is retrospective, that selection bias is inevitable, and that this study has limitations for assessing rupture risk. To predict the actual rupture risk, the ideal data should be collected from patients with aneurysms that are "about to rupture but have not yet ruptured." However, such samples are rare. (1) Most patients are sent to the hospital with ruptured aneurysms, and few opportunities are provided to obtain aneurysm samples before rupture. (2) For patients with aneurysms, doctors may perform surgery when they judge that the aneurysm is likely to rupture, and this cannot be recognized as a sample "to be ruptured but not yet ruptured" because it is not possible to know whether the aneurysm will eventually rupture if it is not treated. One imperfect but practical way is to use ruptured cases as samples at risk of rupture for training and testing based on the assumption that the geometric features of aneurysms will not change after rupture. The prediction probability of the ruptured status still provides helpful information about the rupture risk. Many related papers in the literature adopt the same settings as we did in this paper.[9,31,33,50,51] Although the assumption may not be true for all aneurysms, as mentioned in the literature,[52,53] it is likely to hold for most aneurysms in real-world data, or the changes in most

Table 10. Comparison of clinical diagnosis and TransIAR on the balanced test set

Doctor	Accuracy (95% CI)	AUC (95% CI)	Time
Doctor[1]	82.90 (74.75–91.05)	73.20 (62.00–84.30)	57 min
Doctor[2]	87.80 (80.72–94.88)	76.80 (66.20–87.40)	62 min
TransIAR	89.02 (82.25–95.79)	**92.15 (85.97–98.33)**	**3.46 s**
TransIAR[AF]	**91.46 (85.41–97.51)**	92.09 (85.89–98.29)	3.47 s

TransIAR[AF] means adding auxiliary features (AFs) for training. The best results are shown in bold. In the clinical experiment, the measured morphological features are provided to doctors, so the diagnosis time of doctors does not include the measurement time. It usually takes 10–20 min to measure the morphological characteristics of each patient. The time spent by TransIAR does not include data preprocessing time. It takes an average of 50 s to preprocess the CTA data of each patient.

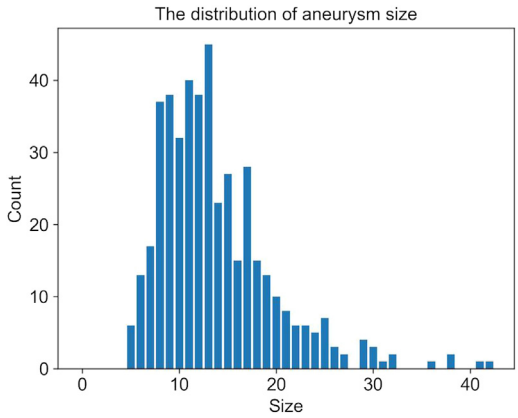

Figure 4. The distribution of aneurysm size (in the unit of voxels) of the entire dataset

The average is 13.78 voxels.

ruptured aneurysms are very small. For example, related literature[54,55] indicates that the morphology of aneurysms basically does not change before and after rupture. After the aneurysm ruptures, the adjacent parent artery may continue to supply blood. Bleeding may be blocked, and thus the morphology of the aneurysm before and after rupture barely changes.

Additionally, the number of unruptured samples is much smaller than that of ruptured samples. Most of the cases come from patients who went to the hospital for examination after having severe symptoms of a ruptured aneurysm. Only a few cases are from patients whose aneurysms were detected before rupture. One possible way to remedy the selection bias is causal analysis methods.

EXPERIMENTAL PROCEDURES

Resource availability

Lead contact

The lead contact is Shikui Tu (tushikui@sjtu.edu.cn).

Materials availability

There are no newly generated materials.

Data and code availability

We provide a test set at Zenodo (https://doi.org/10.5281/zenodo.7536330) for the reviewer to run the test for review. The data in the test set have been preprocessed to be in the same format as the input to our model and the implemented baselines. The AFs for the test set are also given at Zenodo (https://doi.org/10.5281/zenodo.7536330).

Please note that the test set is only used to verify our model during the review process. Because of hospital regulation restrictions and patient privacy concerns, the CTA image data of the patients are only available upon request for academic purposes.

The source code for training and testing has been released at Zenodo (https://doi.org/10.5281/zenodo.7536386) and in the GitHub repository (https://github.com/CMACH508/TransIAR).

Overview of the proposed network

An overview of the proposed TransIAR net is given in Figure 6. The architecture contains three components: (1) a BranchNet module to extract 3D scale-invariant features of IAs from multiple scales, (2) a transformer module to capture dependencies between the aneurysm and its surrounding related anatomic structures, and (3) a feature fusion module to fuse aneurysm data features and AFs to increase the discriminative power. Specifically, the two branches in BranchNet have the same structure, consisting of 3D convolution, rectified linear unit (ReLU), dropout, and max-pooling layers. After concatenating the output of the two branches and performing linear projection, it is sent to the transformer module, which is composed of four encoders, each of which has four heads, and the dimension of each head is 256. The output features then go through the fully connected (FC) and ReLU layers for feature fusion with auxiliary information. Finally, the classification result is obtained through the prediction layers.

BranchNet module

We devise the BranchNet module to extract features of aneurysms of different scales and forms, including large and small sizes, and, more importantly, to learn the representations of IA neighborhood information. The module contains two branches for IA neighborhoods of various sizes. In one branch, a data cube $x_1 \in \mathbb{R}^{48\times48\times48}$ is cropped from the 3D CTA data around the IA's center. We obtain a follow-up data cube, $\tilde{x}_1 \in \mathbb{R}^{48\times48\times48}$ from x_1, by taking a point in the aneurysm as the starting point and using the BFS method to connect all of the pixels. As a result, the IA and its parent arteries are preserved in $\tilde{x}_1$ with the removal of surrounding vascular information of nonparent arteries. Ideally, x_1 already contains the information of $\tilde{x}_1$, and it should be sufficient as the input to the deep CNN for automatic feature extraction. In practice, it would be difficult for the 3D CNN to learn the IA's own geometry and its surrounding anatomic structures from x_1 only because an IA is a relatively small 3D object drowned in the data cube. Hence, we take x_1 and $\tilde{x}_1$ as a two-channel input, and the data cube $\tilde{x}_1$, which contains the IA and

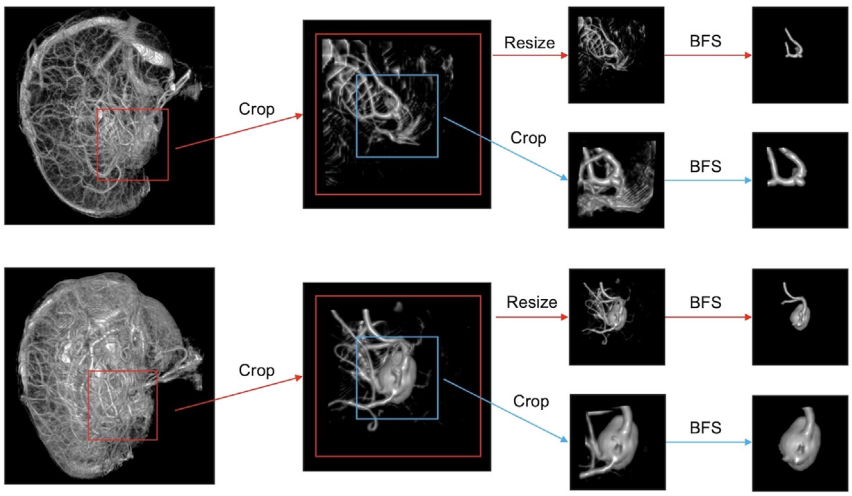

Figure 5. Two examples of cropping an IA and its cubic neighborhood from the 3D CTA data

The blue and red squares indicate neighborhood sizes of 48 and 96 voxels.

Table 11. The impact of IA neighborhood on prediction performance

Size	BFS	Accuracy (95% CI)	Precision	Recall	AUC	AUPR	F1 score
48	Y	69.51 (59.55–79.47)	**90.00**	43.90	74.54	78.18	59.02
96	Y	71.95 (62.23–81.67)	72.50	70.73	74.36	75.89	71.60
48	N	82.93 (74.79–91.07)	78.72	90.24	85.31	82.10	84.09
96	N	85.37 (77.72–93.02)	79.59	**95.12**	92.86	93.20	86.67
48+48	Y+N	84.15 (76.25–92.05)	80.43	90.24	89.35	90.51	85.06
96+96	Y+N	87.80 (80.72–94.88)	86.05	90.24	**93.22**	**93.99**	88.10
48+48+96+96	Y+N+Y+N	**89.02 (82.25–95.79)**	88.10	90.24	92.15	93.16	**89.16**

The results are obtained on balanced datasets in the absence of AFs. The symbol "+" indicates combinations of input data. "Y" and "N" represent "yes" and "no," respectively. For example, the setting "48 + 48, Y + N" denotes taking both "48, Y" and "48, N" as input. The best results are shown in bold.

its parent artery, is a helpful supplement to enhance the representation learning on the geometry of the IA, such as aneurysm size, neck width, and the widths of the parent artery and the nonparent artery.

Although x_1 contains the entire aneurysm and part of the surrounding anatomic structures, the surrounding information may not be sufficient for aneurysms with large sizes. In the other branch, a data cube of size 96×96×96 is cropped from the 3D CTA data around the IA's center and downsampled to $x_2 \in \mathbb{R}^{48\times48\times48}$. Similarly, x_2 is processed by BFS to obtain $\bar{x}_2$, and x_2 and $\bar{x}_2$ are used in deep learning. The two branches enable a multiscale capacity of deep representation learning. To summarize, we have

$$\begin{aligned} b_i &= BranchNet_i(x_i, \bar{x}_i), i = 1, 2; \\ b &= Concat(b_1, b_2), \end{aligned} \quad \text{(Equation 1)}$$

where the two branches have the identical structure as the convolutional part of VoxNet,[56] $C(32,5,2) - C(32,3,1)) - P(2)$, and "Concat" denotes the concatenation operator, $C(f,d,s)$ indicates f filters of size d and at stride s, and $P(m)$ indicates pooling with area m. Note that b is the embedding output by the BranchNet module, and we still keep it as 3D cubes in multiple channels. Because the centers of the input data cubes x_1 and x_2 are always constrained to be the center of the IA, the representations of the IA and its neighborhood are also around the center of the CNN embedding b.

Transformer module

Note that the 3D CNN embedding b in Equation 1 spatially corresponds to the data cubes x_1 and x_2; i.e., the inner volume around b's center is mostly the geometry features of the IA, while the outer volume mainly represents the IA neighborhood features. It allows us to further capture the spatial dependence of the local features in b, which are obviously not independent from each other. As illustrated in Figure 6, we divide b into a sequence of equal-sized small cubic patches and introduce a transformer[57] to extract the patterns in the patch sequence. The self-attention mechanism enables the central aneurysm patch to exchange information with the surrounding vascular patches and improves the learned representations of the IA and its neighborhood.

Concretely, similar to the operation of Vision Transformer (ViT)[58] on 2D images, we divide $b \in \mathbb{R}^{C\times L\times L\times L}$ into a sequence of $P\times P\times P$ patches in each channel, where C is the number of channels. Patches of each channel in the same position are concatenated and flattened to $m_i \in \mathbb{R}^{C\cdot P^3}$ and mapped to a fixed dimension d with a trainable linear projection. Then, we obtain a sequence of embedded patches with length $N = (L/P)^3$. Similar to [class] token of bidirectional encoder representations from transformers (BERT),[59] an extra learnable class embedding e_{class} is attached to the sequence. To retain positional information, standard learnable 1D position embeddings are added to the sequence of embeddings. Finally, we formulate the input of the Transformer module as

$$h = [e_{class}; m_1A; m_2A; \cdots; m_NA] + E_{pos}, \quad \text{(Equation 2)}$$

where $A \in \mathbb{R}^{(C\cdot P^3)\times d}$ is the linear projection matrix, and $E_{pos} \in \mathbb{R}^{(N+1)\times d}$ is the standard learnable 1D position embedding.

Then, h is sent to the transformer encoder to calculate $t \in \mathbb{R}^{256}$, and t is post-processed by the dropout, FC, and LeakyReLU layers to compute the final features of the aneurysm:

$$\begin{aligned} t &= Transformer(h), \\ t_1 &= LeakyReLU(FC(Dropout(t))), \end{aligned} \quad \text{(Equation 3)}$$

where $t_1 \in \mathbb{R}^8$ represents the final extracted aneurysm features. The detailed network structure of the transformer encoder is given at the bottom right corner of Figure 6. The self-attention mechanism can integrate all information of relevant patches into the patch being processed by the model. It should be noted that t_1 in Equation 3 collects the end-to-end automatically learned features, and it can be used to replace the manually measured features by neuroradiologists for rupture prediction.

Feature fusion module

The features of aneurysms and their surrounding structures can be extracted from the 3D CTA images by the BranchNet module and transformer module as in Equation 3, and they are ready to be used to build a classifier for rupture prediction. In addition, some characteristics can be easily obtained by neuroradiologists through simple observation of the aneurysm without shape, location, and other precise measurements. Moreover, certain characteristics, such as patient age, are not included in the CTA images but are related to the aneurysm rupture risk. These AFs are complementary to the IA features learned by the deep neural networks. Therefore, on the basis of aneurysm data, we add AFs $x_3 \in \mathbb{R}^5$ to help network prediction. In general, the AFs are flexible to include any newly found features according to the research on predicting IA rupture status.

The AFs are incorporated via a feature fusion module including Auxiliary net (AuxNet) and Fusion operation. AuxNet extracts AFs x_3 to obtain t_2, and it consists of the FC layer and ReLU activation function. Finally, $t_1 \in \mathbb{R}^8$ by Equation 3 and $t_2 \in \mathbb{R}^{10}$ are concatenated to obtain the fused feature vector $f \in \mathbb{R}^{18}$ as follows:

$$\begin{aligned} t_2 &= AuxNet(x_3), \\ f &= Concat(t_1, t_2). \end{aligned} \quad \text{(Equation 4)}$$

Then, the final prediction is computed through the following network process:

$$\begin{aligned} z &= LeakyReLU(FC(Dropout(f))), \\ s &= FC(Dropout(z)), \end{aligned} \quad \text{(Equation 5)}$$

where $s \in \mathbb{R}^2$ refers to the logit probability of ruptured and unruptured.

Loss function

The aneurysm rupture prediction is actually a binary classification problem. We train our model by minimizing the cross entropy loss function:

$$Loss = -\frac{1}{N_s}\sum_{i=1}^{N_s}\log p_i = -\frac{1}{N_s}\sum_{i=1}^{N_s}\log\frac{e^{s_{y_i}}}{\sum_{j=1}^{N_c}e^{s_j}}, \quad \text{(Equation 6)}$$

where p_i represents the probability of the i-th sample belonging to its target class y_i, N_s and N_c denote the total number of samples and the number of

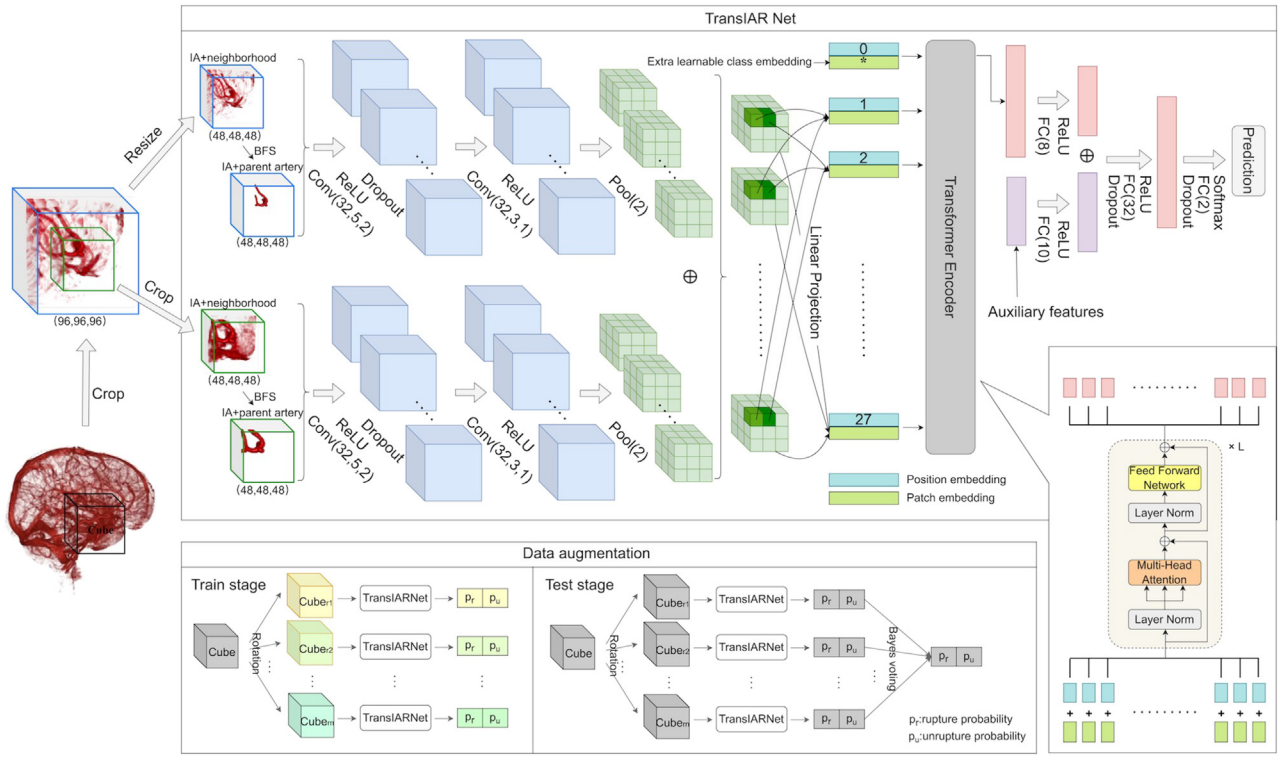

Figure 6. An overview of the TransIAR network
It includes the BranchNet module, transformer module, and feature fusion module.

categories, respectively, and $s = [s_1, s_2]$ represents the logit output of the last FC layer by Equation 5. Here, $N_c = 2$ for two classes; i.e., ruptured or unruptured IA.

Experimental settings

The training set was expanded by data augmentation 32 times to 6,400, each as an independent instance. The number of epochs is set to 100, the learning rate is 0.0001, which remains unchanged, and Adam is adopted to optimize our model. During testing, the average (Bayes voting) predicted probability of 32 variants is calculated as the final rupture probability of this sample.

ETHICS APPROVAL AND CONSENT TO PARTICIPATE

This study was approved by the Ethics Committee of the First Affiliated Hospital of Wenzhou Medical University. Because this is a retrospective study, informed consent was waived. In the published codes and data, the patient's relevant information (name, gender, birthday, etc.) was deleted to protect patient privacy.

SUPPLEMENTAL INFORMATION

Supplemental information can be found online at https://doi.org/10.1016/j.patter.2023.100709.

ACKNOWLEDGMENTS

The authors thank reviewers for their valuable suggestions. This work is supported by National Key R&D Program (2018AAA0100700) of the Ministry of Science and Technology of China, the National Natural Science Foundation of China (62172273), the Shanghai Municipal Science and Technology Major Project (2021SHZDZX0102), the SJTU Medical Engineering Cross-cutting Research Foundation (ZH2018ZDA07), and the Wenzhou Major Program of Science and Technology Innovation (ZY2020012).

AUTHOR CONTRIBUTIONS

Conceptualization, S.T., Y.Y., and L.X.; methodology, Y.L., P.L., and S.T.; software, Y.L. and P.L.; formal analysis, P.L., Y.L., and S.T.; investigation, P.L., Y.L., S.T., and J.Z.; resources, S.T., L.X., J.Z., Y.Y., B.Z., and J.W.; data curation, J.Z., P.L., and Y.L.; writing – original draft, P.L. and Y.L.; writing – review & editing, P.L. and S.T.; visualization, Y.L. and P.L.; supervision, S.T. and L.X.; project administration, S.T. and J.Z.; funding acquisition, S.T., Y.Y., B.Z., and L.X.

DECLARATION OF INTERESTS

The authors declare no competing interests.

Received: September 5, 2022
Revised: November 9, 2022
Accepted: February 22, 2023
Published: March 21, 2023

REFERENCES

1. Fehlings, M.G., and Gentili, F. (1991). The association between polycystic kidney disease and cerebral aneurysms. Can. J. Neurol. Sci. *18*, 505–509.
2. Nurmonen, H.J., Huttunen, T., Huttunen, J., Kurki, M.I., Helin, K., Koivisto, T., von und zu Fraunberg, M., Jskelinen, J.E., and Lindgren, A.E. (2017). Polycystic kidney disease among 4,436 intracranial aneurysm patients from a defined population. Neurology *89*, 1852–1859.
3. Germain, D.P. (2007). Ehlers-Danlos syndrome type IV. Orphanet J. Rare Dis. *2*, 32.

4. Tonnessen, B.H., Sternbergh, W.C., III, Mannava, K., and Money, S.R. (2007). Endovascular repair of an iliac artery aneurysm in a patient with Ehlers-Danlos syndrome type IV. J. Vasc. Surg. *45*, 177–179.

5. Brown, R.D., Jr., and Broderick, J.P. (2014). Unruptured intracranial aneurysms: epidemiology, natural history, management options, and familial screening. Lancet Neurol. *13*, 393–404.

6. Thompson, B.G., Brown, R.D., Jr., Amin-Hanjani, S., Broderick, J.P., Cockroft, K.M., Connolly, E.S., Jr., Duckwiler, G.R., Harris, C.C., Howard, V.J., Johnston, S.C.C., et al. (2015). Guidelines for the management of patients with unruptured intracranial aneurysms: a guideline for healthcare professionals from the American Heart Association/American Stroke Association. Stroke *46*, 2368–2400.

7. Lawton, M.T., and Vates, G.E. (2017). Subarachnoid hemorrhage. N. Engl. J. Med. *377*, 257–266.

8. Nieuwkamp, D.J., Setz, L.E., Algra, A., Linn, F.H.H., de Rooij, N.K., and Rinkel, G.J.E. (2009). Changes in case fatality of aneurysmal subarachnoid haemorrhage over time, according to age, sex, and region: a meta-analysis. Lancet Neurol. *8*, 635–642.

9. Kim, H.C., Rhim, J.K., Ahn, J.H., Park, J.J., Moon, J.U., Hong, E.P., Kim, M.R., Kim, S.G., Lee, S.H., Jeong, J.H., et al. (2019). Machine learning application for rupture risk assessment in small-sized intracranial aneurysm. J. Clin. Med. *8*, 683.

10. Van Gijn, J., Kerr, R.S., and Rinkel, G.J.E. (2007). Subarachnoid haemorrhage. Lancet *369*, 306–318.

11. Bonita, R., and Thomson, S. (1985). Subarachnoid hemorrhage: epidemiology, diagnosis, management, and outcome. Stroke *16*, 591–594.

12. Lantigua, H., Ortega-Gutierrez, S., Schmidt, J.M., Lee, K., Badjatia, N., Agarwal, S., Claassen, J., Connolly, E.S., and Mayer, S.A. (2015). Subarachnoid hemorrhage: who dies, and why? Crit. Care *19*, 309.

13. Molyneux, A., Kerr, R., International Subarachnoid Aneurysm Trial ISAT Collaborative Group, Stratton, I., Sandercock, P., Clarke, M., Shrimpton, J., and Holman, R. (2002). International Subarachnoid Aneurysm Trial (ISAT) of neurosurgical clipping versus endovascular coiling in 2143 patients with ruptured intracranial aneurysms: a randomized trial. J. Stroke Cerebrovasc. Dis. *11*, 304–314.

14. Molyneux, A.J., Kerr, R.S.C., Yu, L.-M., Clarke, M., Sneade, M., Yarnold, J.A., and Sandercock, P.; International Subarachnoid Aneurysm Trial ISAT Collaborative Group (2005). International subarachnoid aneurysm trial (ISAT) of neurosurgical clipping versus endovascular coiling in 2143 patients with ruptured intracranial aneurysms: a randomised comparison of effects on survival, dependency, seizures, rebleeding, subgroups, and aneurysm occlusion. Lancet *366*, 809–817.

15. Bo, Z.-H., Qiao, H., Tian, C., Guo, Y., Li, W., Liang, T., Li, D., Liao, D., Zeng, X., Mei, L., et al. (2021). Toward human intervention-free clinical diagnosis of intracranial aneurysm via deep neural network. Patterns *2*, 100197.

16. Jagadeesan, B.D., Delgado Almandoz, J.E., Kadkhodayan, Y., Derdeyn, C.P., Cross, D.T., Chicoine, M.R., Rich, K.M., Zipfel, G.J., Dacey, R.G., and Moran, C.J. (2014). Size and anatomic location of ruptured intracranial aneurysms in patients with single and multiple aneurysms: a retrospective study from a single center. J. Neurointerv. Surg. *6*, 169–174.

17. Abboud, T., Rustom, J., Bester, M., Czorlich, P., Vittorazzi, E., Pinnschmidt, H.O., Westphal, M., and Regelsberger, J. (2017). Morphology of ruptured and unruptured intracranial aneurysms. World Neurosurg. *99*, 610–617.

18. Raghavan, M.L., Ma, B., and Harbaugh, R.E. (2005). Quantified aneurysm shape and rupture risk. J. Neurosurg. *102*, 355–362.

19. Dhar, S., Tremmel, M., Mocco, J., Kim, M., Yamamoto, J., Siddiqui, A.H., Hopkins, L.N., and Meng, H. (2008). Morphology parameters for intracranial aneurysm rupture risk assessment. Neurosurgery *63*, 185–196. discussion 196-7.

20. Wang, G.-x., Liu, J., Chen, Y.-q., Wen, L., Yang, M.-g., Gong, M.-f., and Zhang, D. (2018). Morphological characteristics associated with the rupture risk of mirror posterior communicating artery aneurysms. J. Neurointerv. Surg. *10*, 995–998.

21. Chen, Y., Xing, H., Lin, B., Zhou, J., Ding, S., Wan, J., Yang, Y., Pan, Y., and Zhao, B. (2020). Morphological risk model assessing anterior communicating artery aneurysm rupture: development and validation. Clin. Neurol. Neurosurg. *197*, 106158.

22. Kang, H., Ji, W., Qian, Z., Li, Y., Jiang, C., Wu, Z., Wen, X., Xu, W., and Liu, A. (2015). Aneurysm characteristics associated with the rupture risk of intracranial aneurysms: a self-controlled study. PLoS One *10*, e0142330.

23. Elsharkawy, A., Leheka, M., Niemel, M., Kivelev, J., Billon-Grand, R., Lehto, H., Kivisaari, R., and Hernesniemi, J. (2013). Anatomic risk factors for middle cerebral artery aneurysm rupture: computed tomography angiography study of 1009 consecutive patients. Neurosurgery *73*, 825–837. discussion 836-7.

24. Liu, Q., Jiang, P., Jiang, Y., Ge, H., Li, S., Jin, H., and Li, Y. (2019). Prediction of aneurysm stability using a machine learning model based on PyRadiomics-derived morphological features. Stroke *50*, 2314–2321.

25. Matsukawa, H., Uemura, A., Fujii, M., Kamo, M., Takahashi, O., and Sumiyoshi, S. (2013). Morphological and clinical risk factors for the rupture of anterior communicating artery aneurysms. J. Neurosurg. *118*, 978–983.

26. Richardson, A.E., Jane, J.A., and Payne, P.M. (1964). Assessment of the natural history of anterior communicating aneurysms. J. Neurosurg. *21*, 266–274.

27. Baharoglu, M.I., Schirmer, C.M., Hoit, D.A., Gao, B.-L., and Malek, A.M. (2010). Aneurysm inflow-angle as a discriminant for rupture in sidewall cerebral aneurysms: morphometric and computational fluid dynamic analysis. Stroke *41*, 1423–1430.

28. Amenta, P.S., Yadla, S., Campbell, P.G., Maltenfort, M.G., Dey, S., Ghosh, S., Ali, M.S., Jallo, J.I., Tjoumakaris, S.I., Gonzalez, L.F., et al. (2012). Analysis of nonmodifiable risk factors for intracranial aneurysm rupture in a large, retrospective cohort. Neurosurgery *70*, 693–699. discussion 699-701.

29. Ujiie, H., Tamano, Y., Sasaki, K., and Hori, T. (2001). Is the aspect ratio a reliable index for predicting the rupture of a saccular aneurysm? Neurosurgery *48*, 495–502. discussion 502-3.

30. International Study of Unruptured Intracranial Aneurysms Investigators (1998). Unruptured intracranial aneurysms—risk of rupture and risks of surgical intervention. N. Engl. J. Med. *339*, 1725–1733.

31. Liu, J., Chen, Y., Lan, L., Lin, B., Chen, W., Wang, M., Li, R., Yang, Y., Zhao, B., Hu, Z., and Duan, Y. (2018). Prediction of rupture risk in anterior communicating artery aneurysms with a feed-forward artificial neural network. Eur. Radiol. *28*, 3268–3275.

32. Zhu, W., Li, W., Tian, Z., Zhang, Y., Wang, K., Zhang, Y., Liu, J., and Yang, X. (2020). Stability assessment of intracranial aneurysms using machine learning based on clinical and morphological features. Transl. Stroke Res. *11*, 1287–1295.

33. Detmer, F.J., Chung, B.J., Mut, F., Slawski, M., Hamzei-Sichani, F., Putman, C., Jimnez, C., and Cebral, J.R. (2018). Development and internal validation of an aneurysm rupture probability model based on patient characteristics and aneurysm location, morphology, and hemodynamics. Int. J. Comput. Assist. Radiol. Surg. *13*, 1767–1779.

34. Detmer, F.J., Lckehe, D., Mut, F., Slawski, M., Hirsch, S., Bijlenga, P., von Voigt, G., and Cebral, J.R. (2020). Comparison of statistical learning approaches for cerebral aneurysm rupture assessment. Int. J. Comput. Assist. Radiol. Surg. *15*, 141–150.

35. Wang, H., Li, W., He, H., Luo, L., Chen, C., and Guo, Y. (2013). 320-detector row CT angiography for detection and evaluation of intracranial aneurysms: comparison with conventional digital subtraction angiography. Clin. Radiol. *68*, e15–e20.

36. Sugiu, K., Jean, B., San Millan Ruiz, D., Martin, J.B., Delavelle, J., and Rfenacht, D.A. (2000). Influence of the perianeurysmal environment on rupture of cerebral aneurysms preliminary observation. Interv. Neuroradiol. *6*, 65–70.

37. San Millán Ruíz, D., Yilmaz, H., Dehdashti, A.R., Alimenti, A., De Tribolet, N., and Rfenacht, D.A. (2006). The perianeurysmal environment: influence

on saccular aneurysm shape and rupture. AJNR. Am. J. Neuroradiol. *27*, 504–512.

38. Backes, D., Vergouwen, M.D.I., Velthuis, B.K., van der Schaaf, I.C., Bor, A.S.E., Algra, A., and Rinkel, G.J.E. (2014). Difference in aneurysm characteristics between ruptured and unruptured aneurysms in patients with multiple intracranial aneurysms. Stroke *45*, 1299–1303.

39. Guo, Y., Huang, W., Chen, Y., and Tu, S. (2019). Regularize network skip connections by gating mechanisms for electron microscopy image segmentation. In 2019 IEEE International Conference on Multimedia and Expo (ICME), pp. 868–873.

40. Wang, W., Chen, C., Ding, M., Yu, H., Zha, S., and Li, J. (2021). Transbts: multimodal brain tumor segmentation using transformer. In International Conference on Medical Image Computing and Computer-Assisted Intervention, pp. 109–119.

41. Zhang, Y., He, N., Yang, J., Li, Y., Wei, D., Huang, Y., Zhang, Y., He, Z., and Zheng, Y. (2022). mmFormer: multimodal medical transformer for incomplete multimodal learning of brain tumor segmentation. Preprint at arXiv. https://doi.org/10.48550/arXiv.2206.02425.

42. Shi, Z., Miao, C., Schoepf, U.J., Savage, R.H., Dargis, D.M., Pan, C., Chai, X., Li, X.L., Xia, S., Zhang, X., et al. (2020). A clinically applicable deep-learning model for detecting intracranial aneurysm in computed tomography angiography images. Nat. Commun. *11*, 6090.

43. Dai, X., Huang, L., Qian, Y., Xia, S., Chong, W., Liu, J., Di Ieva, A., Hou, X., and Ou, C. (2020). Deep learning for automated cerebral aneurysm detection on computed tomography images. Int. J. Comput. Assist. Radiol. Surg. *15*, 715–723.

44. Ma, R., Tu, S., Li, P., Zhou, J., Zhao, B., Wan, J., and Xu, L. (2021). Enriching computed tomography images by projection for robust automated cerebral aneurysm detection and segmentation. In 2021 IEEE International Conference on Bioinformatics and Biomedicine (BIBM), pp. 1026–1031.

45. Jang, J., and Hwang, D. (2022). M3T: three-dimensional medical image classifier using multi-plane and multi-slice transformer. In Proceedings of the IEEE/CVF Conference on Computer Vision and Pattern Recognition (CVPR), pp. 20718–20729.

46. Gainza, P., Sverrisson, F., Monti, F., Rodol, E., Boscaini, D., Bronstein, M.M., and Correia, B.E. (2020). Deciphering interaction fingerprints from protein molecular surfaces using geometric deep learning. Nat. Methods *17*, 184–192.

47. Xiao, C., and Wachs, J. (2021). Triangle-net: towards robustness in point cloud learning. In Proceedings of the IEEE/CVF Winter Conference on Applications of Computer Vision, pp. 826–835.

48. Bronstein, M.M., Bruna, J., LeCun, Y., Szlam, A., and Vandergheynst, P. (2017). Geometric deep learning: going beyond euclidean data. IEEE Signal Process. Mag. *34*, 18–42.

49. Gerken, J.E., Aronsson, J., Carlsson, O., Linander, H., Ohlsson, F., Petersson, C., and Persson, D. (2021). Geometric Deep Learning and Equivariant Neural Networks. CoRR abs/2105.13926.

50. Elsharkawy, A., Leheka, M., Niemel, M., Billon-Grand, R., Lehto, H., Kivisaari, R., and Hernesniemi, J. (2013). A new, more accurate classification of middle cerebral artery aneurysms: computed tomography angiographic study of 1009 consecutive cases with 1309 middle cerebral artery aneurysms. Neurosurgery *73*, 94–102. discussion 102.

51. Zhou, J., Xia, N., Li, Q., Zheng, K., Jia, X., Wang, H., Zhao, B., Liu, J., Yang, Y., and Chen, Y. (2022). Predicting the rupture status of small middle cerebral artery aneurysms using random forest modeling. Front. Neurol. *13*, 921404.

52. Chien, A., and Sayre, J. (2014). Morphologic and hemodynamic risk factors in ruptured aneurysms imaged before and after rupture. AJNR. Am. J. Neuroradiol. *35*, 2130–2135.

53. Cornelissen, B.M.W., Schneiders, J.J., Potters, W.V., Van Den Berg, R., Velthuis, B.K., Rinkel, G.J.E., Slump, C.H., VanBavel, E., Majoie, C.B.L.M., and Marquering, H.A. (2015). Hemodynamic differences in intracranial aneurysms before and after rupture. AJNR. Am. J. Neuroradiol. *36*, 1927–1933.

54. Rahman, M., Ogilvy, C.S., Zipfel, G.J., Derdeyn, C.P., Siddiqui, A.H., Bulsara, K.R., Kim, L.J., Riina, H.A., Mocco, J., and Hoh, B.L. (2011). Unruptured cerebral aneurysms do not shrink when they rupture: multicenter collaborative aneurysm study group. Neurosurgery *68*, 155–160. discussion 160-1.

55. Yi, J., Zielinski, D., and Chen, M. (2016). Cerebral aneurysm size before and after rupture: case series and literature review. J. Stroke Cerebrovasc. Dis. *25*, 1244–1248.

56. Maturana, D., and Scherer, S. (2015). Voxnet: a 3d convolutional neural network for real-time object recognition. In 2015 IEEE/RSJ International Conference on Intelligent Robots and Systems (IROS), pp. 922–928.

57. Vaswani, A., Shazeer, N., Parmar, N., Uszkoreit, J., Jones, L., Gomez, A.N., Kaiser, u., and Polosukhin, I. (2017). Attention is all you need. Adv. Neural Inf. Process. Syst. *30*.

58. Dosovitskiy, A., Beyer, L., Kolesnikov, A., Weissenborn, D., Zhai, X., Unterthiner, T., Dehghani, M., Minderer, M., Heigold, G., Gelly, S., et al. (2020). An image is worth 16x16 words: transformers for image recognition at scale. Preprint at arXiv. https://doi.org/10.48550/arXiv.2010.11929.

59. Devlin, J., Chang, M.-W., Lee, K., and Toutanova, K. (2018). Bert: pre-training of deep bidirectional transformers for language understanding. Preprint at arXiv. https://doi.org/10.48550/arXiv.1810.04805.